AGU PUBLICATIONS

JGR

Journal of Geophysical Research: Space Physics

RESEARCH ARTICLE
10.1002/2017JA024582

Key Points:
- Oxygen ion loss from the ionosphere of Mars is mainly driven by magnetic forces generated by the solar wind interaction
- Global ion loss from Mars scales approximately as the square root of both the upstream solar wind pressure and solar ionizing photon flux
- Ion flow speeds in the ionosphere increase with altitude and with solar wind pressure

Correspondence to:
T. E. Cravens,
cravens@ku.edu

Citation:
Cravens, T. E., Hamil, O., Houston, S., Bougher, S., Ma, Y., Brain, D. & Ledvina, S. (2017). Estimates of ionospheric transport and ion loss at Mars. *Journal of Geophysical Research: Space Physics*, *122*, 10,626–10,637. https://doi.org/10.1002/2017JA024582

Received 10 JUL 2017
Accepted 24 SEP 2017
Accepted article online 29 SEP 2017
Published online 14 OCT 2017

Estimates of Ionospheric Transport and Ion Loss at Mars

T. E. Cravens[1], O. Hamil[1], S. Houston[1], S. Bougher[2], Y. Ma[3], D. Brain[4], and S. Ledvina[5]

[1]Department of Physics and Astronomy, University of Kansas, Lawrence, KS, USA, [2]Department of Climate and Space Sciences and Engineering, University of Michigan, Ann Arbor, MI, USA, [3]Institute of Geophysics and Planetary Physics, University of California, Los Angeles, CA, USA, [4]Laboratory for Atmospheric and Space Physics, University of Colorado, Boulder, CO, USA, [5]Space Sciences Laboratory, University of California-Berkeley, Berkeley, CA, USA

Abstract Ion loss from the topside ionosphere of Mars associated with the solar wind interaction makes an important contribution to the loss of volatiles from this planet. Data from NASA's Mars Atmosphere and Volatile Evolution mission combined with theoretical modeling are now helping us to understand the processes involved in the ion loss process. Given the complexity of the solar wind interaction, motivation exists for considering a simple approach to this problem and for understanding how the loss rates might scale with solar wind conditions and solar extreme ultraviolet irradiance. This paper reviews the processes involved in the ionospheric dynamics. Simple analytical and semiempirical expressions for ion flow speeds and ion loss are derived. In agreement with more sophisticated models and with purely empirical studies, it is found that the oxygen loss rate from ion transport is about 5% (i.e., global O ion loss rate of $Q_{ion} \approx 4 \times 10^{24}$ s^{-1}) of the total oxygen loss rate. The ion loss is found to approximately scale as the square root of the solar ionizing photon flux and also as the square root of the solar wind dynamic pressure. Typical ion flow speeds are found to be about 1 km/s in the topside ionosphere near an altitude of 300 km on the dayside. Not surprisingly, the plasma flow speed is found to increase with altitude due to the decreasing ion-neutral collision frequency.

1. Introduction

The loss of oxygen and other volatiles from the atmosphere of Mars is the key driver of the evolution of the atmosphere, and the MAVEN mission is making major advances in our understanding of the loss processes (cf. Jakosky et al., 2015). A major loss process is the photochemical escape of O due to the dissociative recombination of O_2^+ ions that are present in the exosphere. Many papers have been devoted to this topic (see Cravens et al., 2017; Lillis et al., 2015, 2017, and Fox & Hać, 2014, and the many references therein). Another loss mechanism is transport of ions from the planet. Some of the ions created by ionization processes in the upper atmosphere are accelerated to escape speeds via processes associated with the solar wind interaction with the planet (e.g., pickup ions and fast day to night ionospheric flow). This topic has also been extensively studied and has been the subject of several MAVEN investigations (cf. Brain et al., 2015).

Cravens et al. (2017) used a simple approach to finding expressions for photochemical loss of atomic oxygen via dissociative recombination of ionosphere O_2^+ ions. The global loss rate estimated was $Q_O \approx 8 \times 10^{25}$ s^{-1} (I/I_0), where I_0 is the solar maximum solar EUV irradiance (actually, the atomic oxygen ionization frequency can be used here). A key assumption was that almost any ionization event results in O_2^+ production and thus to loss of O if the ionization event takes place in the exosphere. In the chemically controlled part of the exosphere, the loss will be photochemical (e.g., dissociative recombination reactions), but some ions could also be lost via ion transport. In this paper, we estimate the location in the topside dayside ionosphere of the transport/chemistry transition for ionospheric plasma and we assume that ions created above this transition level are lost due to transport rather than to the photochemical loss mechanism. Note that in either case, the oxygen is lost from the atmosphere. We do not consider the detailed ion acceleration mechanisms that actually provide the ions with the escape velocity (e.g., Brecht & Ledvina, 2014; Dong et al., 2014; Ma et al., 2004). We also estimate how the ion loss scales with solar EUV irradiance and with solar wind dynamic pressure.

An implicit assumption in the current paper is that the ions that are controlled by transport processes at high altitudes are eventually lost either by (1) some unspecified acceleration process at high altitude (e.g., ion pickup) for loss out the tail or (2) transport to the nightside, where the O_2^+ can recombine, also causing

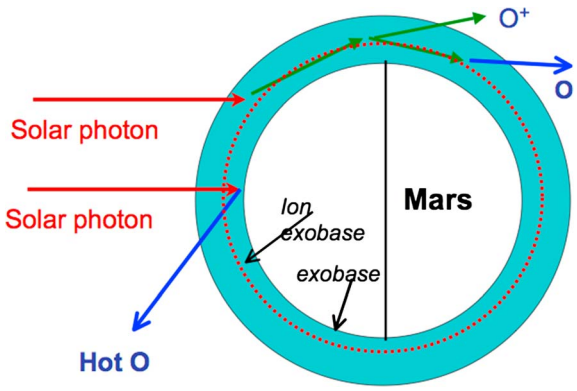

Figure 1. Schematic of the Martian upper atmosphere and ionosphere, illustrating the region of photochemical O production above the exobase and the region of ion loss from day to night above the ion exobase.

loss of O atoms. Figure 1 is a schematic showing ions being created, plasma flow toward the night, and oxygen escape.

In the process of estimating ion escape rates we will also derive simple, approximate expressions for plasma flow speeds in the topside dayside ionosphere that could prove useful for interpreting future MAVEN data and output from global models of the solar wind interaction with Mars.

2. Production of Ions at Mars and Ionospheric Chemistry

The loss of oxygen, either by the photochemical mechanism or by ion loss, requires that the neutral gas be ionized by solar radiation or by fast particles. The major neutral species in the thermosphere of Mars is CO_2, although atomic oxygen is the major neutral species at higher altitudes (Benna et al., 2015; Bougher, Pawlowski, et al., 2015; Mahaffy et al., 2015; Rahmati et al., 2015). See Figure 1. Photoionization of neutrals by solar EUV and soft X-ray radiation is represented by these reactions:

$$\begin{aligned} h\nu + CO_2 &\rightarrow CO_2^+ + e \\ &\rightarrow CO^+ + O + e \\ &\rightarrow O^+ + CO + e \end{aligned} \quad (1)$$

$$h\nu + O \rightarrow O^+ + e \quad (2)$$

Secondary ionization by photoelectrons also contributes about 10% to the total ionization rate. As discussed by Cravens et al. (2017) and in many other papers, the production rate of photoions can be calculated using standard aeronomical techniques (Schunk & Nagy, 2009). Ionization frequencies (I_s in units of s^{-1} for species s) are the ion production rates divided by the neutral density, and in the higher altitude, optically thin region of the upper atmosphere the ion production rate for species s is just $P_s = I_s\, n_{ns}$, where n_{ns} is the neutral density of the relevant species s. $I_{CO2} = 1.8 \times 10^{-6}\ s^{-1}$ and $6 \times 10^{-7}\ s^{-1}$ at a heliocentric distance of 1 AU and for solar maximum and minimum conditions, respectively (cf. Cravens et al., 2017). Similarly, for atomic oxygen, $I_{Ox} = 7 \times 10^{-7}\ s^{-1}$ and $2.3 \times 10^{-7}\ s^{-1}$ for solar maximum and minimum conditions, respectively. Later we identify $I_{Ox0} = 7 \times 10^{-7}\ s^{-1}$ as a reference value. These 1 AU values need to be scaled to the heliocentric distance of Mars.

CO_2^+ ions react with O to produce O_2^+ ions, which dissociatively recombine, thus producing hot oxygen atoms. O^+ ions can also react with CO_2 to produce O_2^+ ions:

$$CO_2^+ + O \rightarrow O_2^+ + CO \quad (3)$$

$$O^+ + CO_2 \rightarrow O_2^+ + CO \quad (4)$$

$$O_2^+ + e \rightarrow O + O \quad (5)$$

The reaction rate coefficients associated with these reactions are $k_3 = 1.64 \times 10^{-10}\ cm^3\ s^{-1}$, $k_4 = 9.4 \times 10^{-10}\ cm^3\ s^{-1}$, and $\alpha = 1.6 \times 10^{-7}\ (300\ K/T_e)^{55}\ cm^3\ s^{-1}$ for reaction (5) (cf. Fox, 1997, 2009; Fox et al., 2015). In addition, N_2^+ ions produced by ionization of N_2 molecules largely end up as O_2^+ due to ion-neutral chemistry (Fox, 2009; Fox et al., 2015).

Table 1
Topside Neutral and Ionospheric Densities, Flow Speeds, and Time Constants

z (km)	nCO_2 (cm^{-3})	nO (cm^{-3})	nN_2 (cm^{-3})	n_n (cm^{-3})
200	1.20E + 08	8.00E + 07	1.60E + 07	2.16E + 08
225	1.80E + 07	5.00E + 07	7.00E + 06	7.50E + 07
250	6.00E + 06	3.20E + 07	3.00E + 06	4.10E + 07
275	9.00E + 05	1.70E + 07	1.00E + 06	1.89E + 07
300	3.20E + 05	1.00E + 07	5.00E + 05	1.08E + 07
325	1.00E + 05	7.00E + 06	2.50E + 05	7.35E + 06
350	3.00E + 04	3.50E + 06	8.00E + 04	3.61E + 06
400	8.00E + 03	1.00E + 06	7.00E + 03	1.02E + 06
450	3.00E + 03	3.00E + 05	6.00E + 02	3.04E + 05

z (km)	nO^+ (cm^{-3})	nO_2^+ (cm^{-3})	Electrons (cm^{-3})
200	200	20,000	20,200
225	500	7,000	7,500
250	800	5,500	6,300
275	900	2,000	2,900
300	900	1,200	2,100
325	900	800	1,700
350	800	500	1,300
400	600	250	850
450	300	150	450

Table 1 lists some typical values of neutral density (n_n) and electron density (n_e) in the dayside ionosphere from MAVEN data (Benna et al., 2015; Withers et al., 2015). These data are representative of the dayside ionosphere for April 2015 with solar zenith angles in the 40° to 60° range.

3. Ionospheric Dynamics—Simple Theory

The transport, and possible escape, of plasma from the topside ionosphere is in response to the net force on a plasma parcel. Horizontally, the main drivers of the dynamics are magnetic forces and thermal pressure forces. A full understanding of this force balance is complicated and depends on the region of Mars, but one can consider two simple regimes—(1) flow largely perpendicular to the draped magnetic field that is induced in the topside ionosphere by the solar wind interaction and (2) flow mainly parallel to the magnetic field driven by the thermal pressure gradient. We will emphasize the first rather than the second, although both are discussed.

3.1. Single-Fluid Momentum Equation

We need to start by estimating flow speeds in the topside ionosphere. We use a single-fluid approach. The single-fluid plasma momentum equation is (cf. Cravens, 1997; Cravens et al., 2010)

$$\rho\left(\frac{\partial \boldsymbol{u}}{\partial t}+\boldsymbol{u}\cdot\nabla\boldsymbol{u}\right)=-\nabla(p_e+p_i)+\boldsymbol{J}\times\boldsymbol{B}+\rho\boldsymbol{g}-\rho\nu_{\mathrm{in}}(\boldsymbol{u}-\boldsymbol{u}_n) \tag{6}$$

where the plasma mass density is ρ, the flow velocity is **u**, and the acceleration due to gravity is **g**. The neutral flow velocity is denoted $\mathbf{u}_n$, and ν_{in} is the ion-neutral momentum transfer collision frequency. The electron and ion pressures are $p_e = n_e\, k_B\, T_e$ and $p_i = n_e\, k_B\, T_i$, respectively, where n_e is the electron density and k_B is Boltzmann's constant. T_e and T_i are the electron and ion temperatures, respectively. Note that quasi-neutrality is assumed so that the ion density n_i equals the electron density ($n_i = n_e$). **J** is the current density, and **B** is the magnetic field. Ampere's law can be used to write $\mathbf{J}\times\mathbf{B}$ as

$$\boldsymbol{J}\times\boldsymbol{B}=-\nabla\left(\frac{B^2}{2\mu_0}\right)+\frac{1}{\mu_0}\boldsymbol{B}\cdot\nabla\boldsymbol{B} \tag{7}$$

The magnetic pressure is given by $p_B = B^2/2\ \mu_0$. Typical values of T_i and T_e in the topside ionosphere are 1,000 K and 2,000 K, respectively (Ergun et al., 2015, 2016; McFadden et al., 2015). The ion-neutral momentum transfer collision frequency is given by $\nu_{\mathrm{in}} = k_{\mathrm{in}}\, n_n$, where n_n is the neutral density and $k_{\mathrm{in}} \approx 10^{-9}\ \mathrm{cm}^3\ \mathrm{s}^{-1}$.

Numerical global MHD models solve the momentum equation, plus continuity equations and energy equations on a spatial grid. In the current paper, we will simplify the momentum equation and derive analytic expressions for the flow velocity **u**.

3.2. Solar Wind Boundary Condition on Ionosphere

Plasma flow in the topside ionosphere is driven most notably by thermal pressure gradient forces and $\mathbf{J}\times\mathbf{B}$ forces (roughly the same as magnetic pressure gradient forces). Except in regions with large crustal magnetic fields, the topside ionospheric pressure ($p_{\mathrm{top}} = p_e + p_i + p_B$) is constrained at higher altitudes by solar wind conditions. Solar wind dynamic pressure ($p_{\mathrm{sw0}} = \rho_{\mathrm{sw}} u_{\mathrm{sw}}{}^2$) is largely converted to thermal pressure downstream of the bow shock and then mostly converted into magnetic pressure inside the magnetic pileup boundary (MPB) (cf. Brain et al., 2015; Brecht & Ledvina, 2014; Crider et al., 2002, 2003; Edberg et al., 2009; Ma et al., 2015; Modolo et al., 2016) in the magnetic pileup region (MPR).The subsolar magnetic pressure in the MPR (or induced magnetic barrier), p_{B0}, is approximately equal to the upstream solar wind dynamic pressure, p_{sw0}. In the subsolar topside ionosphere, $p_{\mathrm{top}} \approx p_{\mathrm{sw0}} = \rho_{\mathrm{sw}} u_{\mathrm{sw}}{}^2$. The magnetic barrier pressure on the

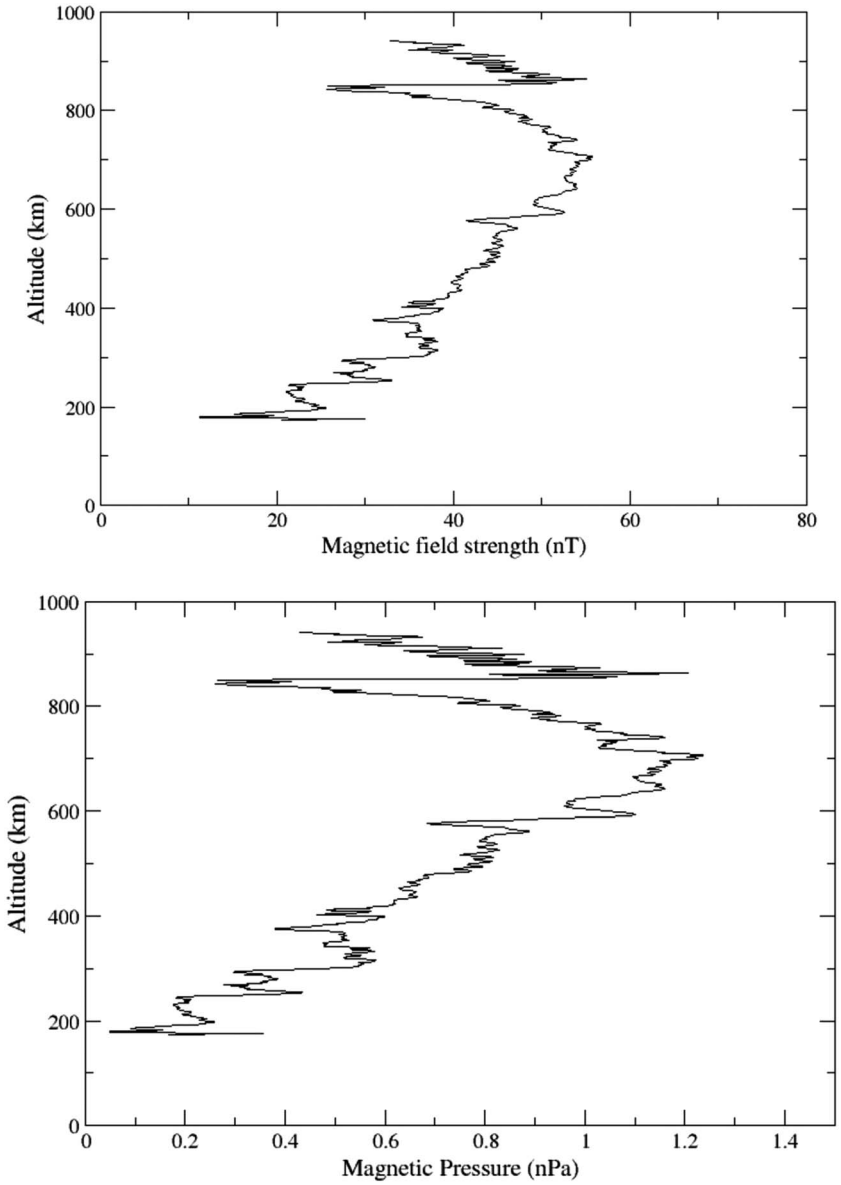

Figure 2. Example of MAVEN magnetometer data in the dayside ionosphere. Magnetic field strength versus altitude for orbit 180. The magnetic pressure near 300 km is about 0.5 nPa.

dayside falls off with solar zenith angle according to MGS data (Akalin et al., 2010; Crider et al., 2003), MAVEN magnetometer data (Connerney et al., 2015), and global interaction models (Ma et al., 2004).

The average magnetic pressure in the topside ionosphere measured by the MGS varies with θ_{mpb}, the angle between the Sun, and the obstacle boundary normal, as (Crider et al., 2003)

$$p_B = p_{\mathrm{sw0}}\ \cos^2\theta_{\mathrm{mpb}} + p_{t0} \tag{8}$$

where p_{s0} is a relatively small pressure. Figure 2 displays a typical dayside magnetic field profile measured by the MAVEN magnetometer (Connerney et al., 2015) for a region without crustal fields. And Figure 3 shows average topside magnetic pressures versus solar zenith angle instead of θ_{mpb} from MGS magnetometer data (Crider et al., 2003). The following approximate expression for the pressure versus solar zenith angle, χ, was found to be reasonable:

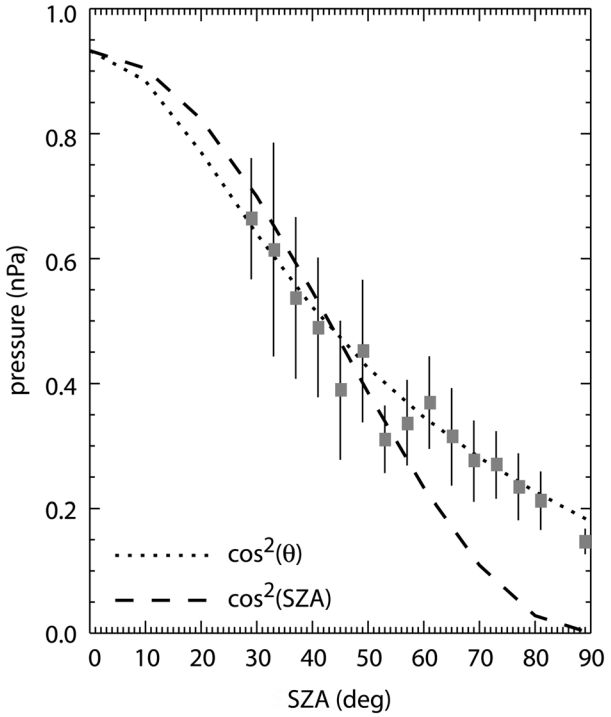

Figure 3. Average magnetic pressure versus solar zenith angle in the magnetic pileup region from Mars Global Surveyor magnetometer data (Crider et al., 2003). The angle between the radius vector and the magnetic pileup boundary surface is θ, but we used the solar zenith angle in the current paper.

$$p_B(\chi) \approx p_{sw0}\left\{0.66\cos^2\chi + 0.33\cos^2(\chi/2)\right\} \quad (9)$$

The total pressure in the topside ionosphere at a given location should be roughly independent of altitude. We express the pressure in terms of physical distance from the subsolar point, s, along a constant radial distance $r = R_M + z$, where R_M is the Martian radius and z is altitude. The incremental distance ds is given by

$$ds = r\,d\chi = (R_M + z)\,d\chi. \quad (10)$$

The horizontal component of the magnetic pressure gradient (or total pressure gradient because magnetic pressure dominates) can be approximately expressed as

$$|\nabla_{hor} p_B| = \frac{1}{R_M + z}\frac{dp_B}{d\chi} \simeq \left[\frac{2p_{sw0}}{R_{eM}}\right]\left\{\frac{2}{3}\sin\chi\cos\chi + \frac{1}{6}\sin\frac{\chi}{2}\cos\frac{\chi}{2}\right\} \quad (11)$$

At locations with $\chi = 60°$ (i.e., middle of the dayside) the term in brackets in the last equation is 0.36. The pressure gradient is roughly $p_{sw0}/(R_M/2)$.

3.3. Simple Single-Fluid MHD Momentum Balance for the Ionosphere

Next, we carry out various approximations to equation (6) and obtain simple expressions for the horizontal plasma flow speed using the horizontal pressure gradient just found. We assume that the vertical component of the flow velocity **u** is much less than the horizontal component. That is, we assume that flow streamlines are largely horizontal on the dayside. We also neglect magnetic tension forces or assume that they are comparable to the magnetic pressure gradient force.

The time-independent horizontal momentum equation can now be written as

$$\rho u\frac{du}{ds} = \frac{-d}{ds}(p_e + p_i + p_B) - \rho\upsilon_{in}(u - u_n) \quad (12)$$

The total pressure is given by $p = p_e + p_i + p_B$. Actually, the last term on the right-hand side is really the component of the $\mathbf{u} - \mathbf{u}_n$ vector along the flow direction, but for simplicity in our estimates, we assume that the neutral and ion velocities are simply in the same (or opposite) directions.

The momentum equation can be further approximated by

$$\frac{d}{ds}\left[\frac{1}{2}u^2 + \frac{p}{\rho}\right] + \upsilon_{in}(u - u_n) = 0 \quad (13)$$

Note that for this last expression $1/\rho$ has been brought inside the derivative by assuming that the plasma density does not vary much with horizontal distance s. Numerical solutions of equation (13) for $u(s)$ (i.e., $u(\chi)$) can be determined at different altitudes and for different solar wind pressures, assuming that $p(s) \approx p_B(s)$ as given by the empirical relation equation (11). See Figures 5 and 6. The solution of equation (13) that is shown assumes that magnetic pressure dominates over thermal pressure and is given by equation (11). Indeed, one empirically finds that in the topside ionosphere for $z \approx$ 300–400 km, the thermal pressure $p_e + p_i \approx n_e k_B (T_e + T_i) \approx 0.15$ nPa for $n_e \approx 2{,}000$ cm^{-3} and for $T_e + T_i \approx 5{,}000$ K (Ergun et al., 2015; Matta et al., 2013; Sakai et al., 2015, 2016; L. Andersson, private communication, 2017), whereas the magnetic pressure

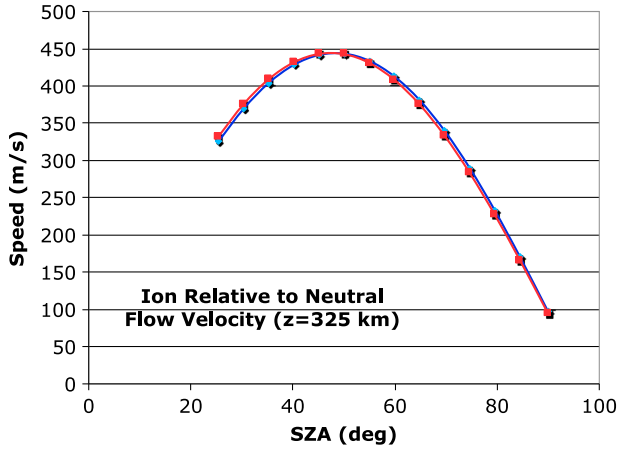

Figure 4. Flow speed versus solar zenith angle from simple MHD theory at 325 km. The red line is from the diffusion (i.e., low altitude) approximation and the blue line from the "full" simple theory.

(Figure 3) is about 4–5 times greater than this. That is, the plasma beta is rather large ($\beta \approx 5$). However, a more careful analysis taking thermal pressure into account could be undertaken in the future.

The results show that flow speeds increase with solar zenith angle generally, out to sza ≈ 60°, and also strongly increase with altitude because the ion-neutral collision term, which opposes the pressure gradient term, rapidly decreases with altitude.

3.4. High-Altitude Approximation

An even more approximate solution can be found at higher altitudes where ion-neutral collisions can be neglected:

$$\frac{1}{2}u^2 + \frac{p}{\rho} = \text{constant} \tag{14}$$

This solution applies along a streamline, assumed to be approximately constant in altitude, and it can be rewritten as

$$u^2 = u_0^2 + \frac{2p_0}{\rho_0} - \frac{2p}{\rho} = u_0^2 + C_{ms0}^2 - C_{ms}^2 \tag{15}$$

The subscript "0" denotes values at the start of a streamline near $s_0 \approx 0$ at the subsolar point. C_{ms} is the magnetosonic speed and $C_{ms} \approx C_A$, where C_A is the Alfven speed. $C_A{}^2 = B^2/\rho\mu_o$ and C_A can be found using the empirical average magnetic field B as a function of s (or θ). With $u_0 \approx 0$ and $C_{ms} \approx 0$ near the terminator ($\theta = 90°$), the terminator plasma flow speed in this approximation is just the subsolar Alfven speed in the magnetic barrier: $u \approx C_{ms0} \approx C_{A0}$.

3.5. Low-Altitude (Ambipolar Diffusion) Approximation

At lower altitudes, we can assume that $u^2 \ll C_{ms}{}^2$ or $M_{ms} \ll 1$, where M_{ms} is the fast mode Mach number. In this case, the ion-neutral friction term balances the pressure gradient term in the momentum equation, and we have the following approximate ambipolar diffusion solution:

$$u - u_n = \frac{-1}{\rho\nu_{in}}\frac{dp}{ds} \tag{16}$$

Letting the neutral flow speed be $u_n \approx 0$, and for $\chi = 60°$, the flow speed from this diffusion approximation becomes

$$u \approx 2.5\times10^{28}\frac{m}{s}\left[\frac{p_{sw}(Pa)}{n_e(m^{-3})n_n(cm^{-3})}\right] \tag{17}$$

The upstream solar wind pressure is p_{sw} (used instead of p_{sw0} after this point in the paper), and the units to be used are indicated. As noted just after equation (11), the horizontal pressure gradient used in equation (16) to get equation (17) was equation (11) with a solar zenith angle of 45°, giving $dp/ds = 0.7(p_{sw}/(R_M/2))$. Typically, near Mars $p_{sw} \approx 1$ nPa. The neutral and electron densities (n_n and n_e, respectively) are needed to find u. Values of n_n and n_e from Table 1 are used to obtain flow speeds and are shown in Figures 4–7.

Figures 5 and 6 show the flow speed from all three methods versus solar zenith angle for several different altitudes. Figure 7 shows flow

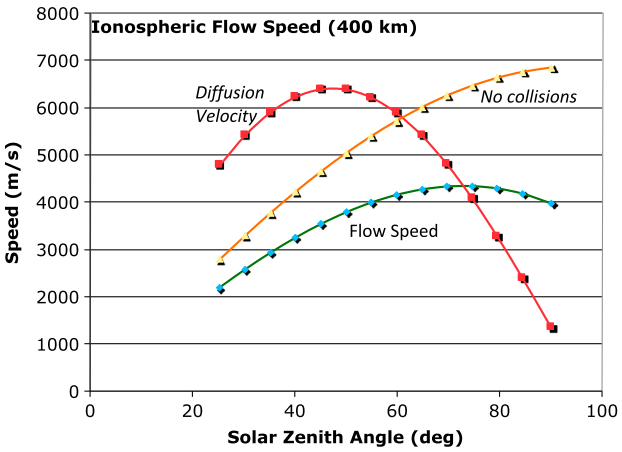

Figure 5. Flow speed versus solar zenith angle from simple MHD theory at 400 km. The red line is from the diffusion (i.e., low altitude) approximation and the blue line from the "full" simple theory.

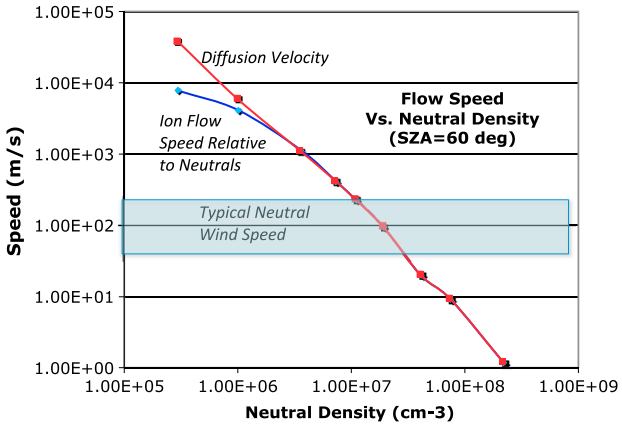

Figure 6. Flow speed versus neutral density for a solar zenith angle of 60°.

speed versus neutral density. An altitude-independent neutral wind speed of $u_n = 100$ m/s in the same direction as the solar wind-driven velocity was adopted. Note that below about 200–225 km the neutral wind speed, u_n, is comparable to $|\mathbf{u}_i - \mathbf{u}_n|$. The neutral wind speed depends on season and location on Mars (Bougher, Pawlowski, et al., 2015; Bougher, Cravens, et al., 2015). Note that the ambipolar diffusion speed from equation (16) or (17) should be a reasonable approximation below about 350–400 km ($n_n < 10^6$ cm^{-3}).

3.6. Plasma Flow Parallel to the Magnetic Field

Parallel to the magnetic field the magnetic pressure gradient force cannot operate and so the thermal pressure gradient force cannot be neglected. Thermal pressure gradient forces move the plasma as indicated by the above simple momentum equations. As stated earlier, a careful analysis of this effect is beyond the scope of the current paper, but a simple estimate is made here. We approximate the horizontal flow speed parallel to the magnetic field as

$$u - u_n = \frac{-\nabla(p_e + p_i)}{\rho \nu_{in}} \approx -\frac{[k_B(T_e + T_i)]}{m_i k_{in} n_n} \frac{1}{n_e} \frac{dn_e}{ds} \tag{18}$$

A horizontal electron variation length scale is defined by $L_e^{-1} \approx (dn_e/ds)/n_e$, and we note that $L_e \approx R_M/2$. In this case, the flow speed is of the order of

$$|\mathbf{u} - \mathbf{u}_n| \approx 300 \text{ km/s } (T_e/n_n) \tag{19}$$

with $\mathbf{u}$ in units of km/s, T_e in units of Kelvin, and the neutral density n_n in units of cm^{-3}. For example, near an altitude of 400 km, where $n_n \approx 10^6$ cm^{-3}, $u \approx 1$ km/s, which is somewhat less than the 6 km/s flow speed found for magnetic pressure gradient forces. The flow speed ratio is just the plasma beta. The scaling of this speed with solar EUV irradiance depends on the scaling of the electron density with solar EUV irradiance.

3.7. Comparison of Simple Dynamical Model With Global Models

The ionospheric flow speeds found for the dayside from the simple analysis are compared with results from global MHD code for comparable conditions and with flow. Figure 7 shows flow speed versus altitude for a solar zenith angle of about 60° for MAVEN conditions. The 3-D MHD model results are from case 1 of Ma et al. (2004). This run was for solar maximum conditions and for normal solar wind conditions (1.2 nPa upstream dynamic pressure) with a 3 nT parker spiral. The IMF direction was in the equatorial plane. The MHD velocity values were extracted at 60° latitude in the XZ (meridional) plane, which is generally consistent with the generic dayside conditions assumed for the analytical solution. Given that conditions were not exactly matched and given the simplicity of the analytic expressions, the agreement is quite good.

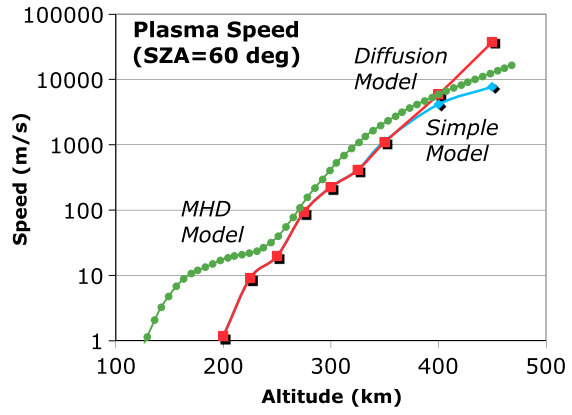

Figure 7. Comparison of analytical flow speed with numerical MHD simulation on the dayside (Ma et al., 2004). The solar zenith angle is 60°.

Further work will be needed to expand on these comparisons with other global models (e.g., Brecht & Ledvina, 2014; Ma et al., 2004, 2015; Modolo et al., 2016) and with ion flow data from NGIMS and STATIC, but this effort is beyond the scope of this initial exploratory work.

4. Ion Transport and Escape

In this section, the approximate flow speeds introduced earlier are used to estimate the transition between a chemically controlled ionosphere and a transport-controlled ionosphere on the dayside. This transition is then used to estimate the ion loss from the planet via a production

rate technique. The transition altitude (or critical level—actually critical total neutral density, n_{nc}) is determined by equating chemical lifetime, for either O^+ or $O_2{}^+$, with transport lifetime.

Once the critical neutral density, n_{nc}, is found, then the total global ion loss rate is just the total ionization rate at higher altitudes:

$$Q \approx I_{Ox}\, n_{nc}\, 2\pi\, H_O\, R_M{}^2 \tag{20}$$

where $H_O \approx 40$ km is the atomic O scale height. Cravens et al. (2017) also discussed this expression. Note that the ionization frequency at the location of Mars must be used. Equation (20) assumes that atomic oxygen is the main neutral species at the relevant altitudes. Next, we find expressions for the critical level/density.

4.1. Plasma Continuity Equation and Chemical Lifetimes

The continuity equation for an ion species, s, in the ionosphere is given by (Schunk & Nagy, 2009, and references therein)

$$\frac{\partial n_s}{\partial t} + \nabla\cdot(n_s \boldsymbol{u}_s) = P_s - L_s \tag{21}$$

A dimensional analysis of this equation indicates that the transport time is $\tau_T \approx L/u$, where L is an appropriate length scale and u is the flow speed. A typical horizontal length scale on the dayside is $L \approx R_M/2$, and horizontal flow speeds were discussed earlier. For vertical transport, the length scale is a vertical scale height, $H \approx H_O$, and a vertical flow speed should be used: (u_z): $\tau_{Tz} \approx H_O/u_z$.

The one-dimensional, multifluid, MHD model of Shinagawa and Cravens (1989) showed that the vertical plasma speed in the Martian ionosphere is $u_z \approx$ 10–20 m/s, and the vertical transport time is $\tau_{Tz} \approx$ 3,000 s. However, in regions with a large radial component of the magnetic field (e.g., crustal magnetic field regions, closed, or cusp), the radial flow speed is very likely to be higher than in draped field regions with consequent lower radial transport times.

Now we consider chemical lifetimes in the ionosphere. The photochemical equilibrium approximation for ion species s is given by $P_s = L_s$, where $L_s = L_s\, n_s$, so that $n_s = P_s/L_s$. An approximate photochemical equilibrium expression for the O^+ density is

$$n_{O+} = I_{Ox}\, n_O/k_4\, n_{CO2} \tag{22}$$

where $n_O{}^+$, n_{CO2}, and n_O are the densities of O^+ ions, CO_2, and O, respectively. A very approximate "empirical" value for the CO_2 density above about 200 km is given in Table 1, in terms of the total neutral density:

$$n_{CO2} \approx n_n{}^2/n_O(z = 210\ \text{km}) \approx 4\times10^{-9}\, n_n{}^2\ \text{cm}^{-3} \tag{23}$$

The O^+ chemical lifetime associated with reaction (22) is $\tau_{cO+} \approx 1/k_2\, n_{CO2}$, when n_{CO2} can be taken from equation (23). Such time constant expressions are obtainable by a dimensional analysis of the relevant ion loss rate (e.g., loss rate (units of $\text{cm}^{-3}\ \text{s}^{-1}$) = $k_2 n_{CO2} n_{O+}$, for O^+ ions) (cf. Schunk & Nagy, 2009).

The photochemical approximation for the $O_2{}^+$ density, assuming only chemical loss by dissociative recombination, is given by

$$n_{O2+} = (P_{O+} + P_{CO2+})/(\alpha\, n_e) \approx P_{O+}/(\alpha\, n_e) \approx I_{Ox}\, n_O/(\alpha\, n_e) \tag{24}$$

The ionization of O dominates the total ionization rate for the topside ionosphere ($z > 200$ km). Further, assuming that $n_e \approx [O_2{}^+]$ below about 300 km, the electron density expression becomes

$$n_e \approx \left(\frac{I_{0x}}{\alpha}\right)^{1/2} n_n^{1/2} \tag{25}$$

With $T_e \approx$ 2,000 K, $\alpha \approx 6\times10^{-8}\ \text{cm}^3\ \text{s}^{-1}$ (Peverall et al., 2001). For MAVEN conditions and for altitudes above 200 km, this expression becomes

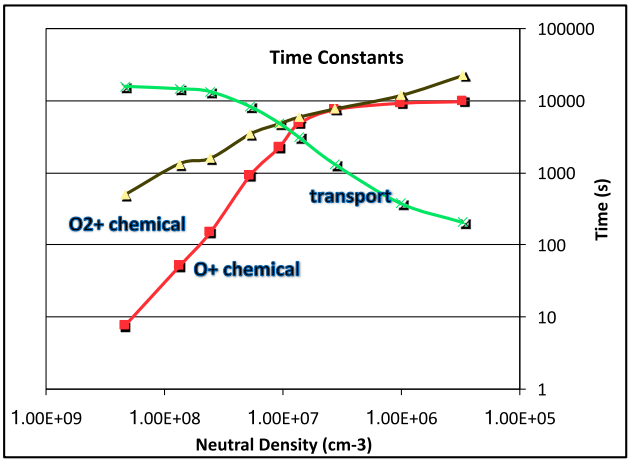

Figure 8. Chemical and transport time constants versus neutral density.

$$n_e \approx 2\, n_n^{1/2} \text{ (with both densities in cgs units)} \tag{26}$$

Using a solar maximum ionization frequency for atomic oxygen one finds that equation (17) for the flow speed, using equation (26) for the electron density, becomes

$$u \approx 1.3\times 10^{22} \frac{m}{s} \frac{p_{sw}}{n_n^{3/2}} \tag{27}$$

where the solar wind pressure is units of Pascals (Pa) and the neutral density, n_n, is in cgs units. Putting in the solar activity and solar wind pressure dependencies gives

$$u \approx 1.3\times 10^{13} \frac{m}{s} \left(\frac{I_{0x0}}{I_{0x}}\right)^{1/2} \left(\frac{p_{sw}}{p_{sw0}}\right) \frac{1}{n_n^{3/2}} \tag{28}$$

Let $I_0 = I_{Ox0}$ be the solar maximum (the reference value) ionization frequency for atomic oxygen and $I = I_{Ox}$ be the ionization frequency at the actual time (and solar activity level). I_{Ox} in equation (25) for the electron density becomes $(I_{Ox}/I_{Ox0})\, I_{Ox0}$ with $I_{Ox0} = 7 \times 10^{-7}\ s^{-1}$ for the solar maximum ionization frequency. The resulting n_e expression is put into equation (17), as well as $p_{sw} = (p_{sw}/p_{sw0})\, p_{sw}$. Equation (28) results from these steps. Note that in terms of the $F_{10.7}$ proxy of solar activity one has $I_0/I \approx 200/F_{10.7}$. Chemical and transport lifetimes are shown as functions of altitude in Figure 8 and in Table 2. Also, in equation (28), a reference solar wind pressure, $p_{sw0} = 10^{-9}$ Pa, was adopted.

4.2. Critical Neutral Density for Ion Transport (Comparison of Time Constants)

An ion "exobase" or transport-chemical transition level can be defined where the chemical and transport times are equal: $\tau_T \approx \tau_{chem}$. Figure 8 displays these time constants plotted versus the neutral density for the density values from Table 1 and for chemical and transport expressions introduced earlier. Table 2 also lists these time constants. The transition density for O^+ ions (n_{ncO+}) is about $10^7\ cm^{-3}$ and for O_2^+ ions is also about $10^7\ cm^{-3}$. The O^+ and O_2 densities are comparable near 300–400 km (Benna et al., 2015). Note that the estimated flow speeds in Table 1, used to estimate transition densities, were found using equation (13) and did not make the low-altitude approximation.

4.3. Analytical Scaling for Transition Level Densities

Now instead of using Table 1 values for ion and electron densities, photochemical expressions found in section 4.2 are used, as well as the low-altitude flow approximation of equation (17) (i.e., equation (28)). This allows purely analytical expressions for the critical neutral densities to be found. Flow speed from equation (28) is used in the transport time expression and equated to the photochemical lifetime of either O^+ or O_2^+. The critical neutral density level for O^+ is given by the expression:

Table 2
Ionospheric Flow Speeds and Time Constants

z (km)	τO^+ (s)	τO_2^+ (s)	u-u_n (m/s)	u_{tot} (m/s)	τ_T (s)
200	7.57E + 00	4.95E + 02	1.17E + 00	1.01E + 02	1.58E + 04
225	5.03E + 01	1.33E + 03	9.10E + 00	1.09E + 02	1.47E + 04
250	1.49E + 02	1.59E + 03	1.97E + 01	1.20E + 02	1.34E + 04
275	9.17E + 02	3.45E + 03	9.31E + 01	1.93E + 02	8.28E + 03
300	2.21E + 03	4.76E + 03	2.26E + 02	3.26E + 02	4.91E + 03
325	4.76E + 03	5.88E + 03	4.13E + 02	5.13E + 02	3.12E + 03
350	7.52E + 03	7.69E + 03	1.13E + 03	1.23E + 03	1.30E + 03
400	9.19E + 03	1.18E + 04	4.15E + 03	4.25E + 03	3.76E + 02
450	9.68E + 03	2.22E + 04	7.71E + 03	7.81E + 03	2.05E + 02

$$ncO + \approx 4\times 10^6 cm^{-3} \left[\frac{I_{0x0}}{I}\right]^{1/7} \left[\frac{p_{sw}}{p_{sw0}}\right]^{2/7} \tag{29}$$

The critical neutral density for O_2^+ is given by

$$ncO2 + \approx 10^{13} cm^{-3} \sqrt{\frac{p_{sw}}{I_{0x0} R_M}} \tag{30}$$

Expressing this equation in terms of the ionization frequency for oxygen and in terms of solar wind pressure relative to the average reference value $p_{sw0} = 10^{-9}$ Pa, it becomes

$$nc\mathrm{O2}+\approx 3\times 10^{6}\,\mathrm{cm}^{-3}\left[\frac{p_{sw}}{p_{sw0}}\right]^{1/2}\left(\frac{I_{0x0}}{I}\right)^{1/2} \tag{31}$$

The solar irradiance, I, comes into equation (31) via the electron density for the chemical loss of O_2^+ as well as through the electron density in expression (17) for the speed (and later equations for the speed derived from this). The critical densities for O^+ and $O_2^+$are both $n_{nc} \approx 4 \times 10^6$ cm^{-3} from equations (30) and (31). Table 1 and Figure 7 give values that are a factor of 2 or so higher than this value. In either case, the corresponding critical altitude is roughly 300–350 km for the MAVEN epoch. Using the low-altitude flow speed expression introduces more uncertainty, but Figure 6 indicates that near the photochemical/transport transition altitude, the low-altitude expression does a fairly good job for the flow speed.

5. Global Ion Escape and Discussion

What happens to ions transported from the dayside to the nightside? Considerable modeling and data analysis have addressed this topic (cf. Brain et al., 2015; Brecht & Ledvina, 2014; Ma et al., 2015; Modolo et al., 2016). Ionospheric plasma transported from the dayside can either supply the nightside ionosphere or the ions can be lost to Mars via "ion escape" out the tail or in the ion plume (cf. Brain et al., 2004, 2015; Fränz et al., 2010). Ions that cross into the nightside can drift/diffuse downward and are ultimately lost via dissociative recombination of O_2^+ ions deeper in the ionosphere, again leading to O escape. Either way most of the ionization produced in the transport region (i.e., above the critical density, n_{nc}, altitude) represents atmospheric loss of O. The supply of ions for the "ion escape" is limited to the neutrals that can be ionized by solar radiation (or by impact ionization due to external electron/ion precipitation) in the transport region above about 300 km.

Equation (20) gives an overall estimate of the ion loss due to ionization of oxygen in the topside ionosphere, but losses via O_2^+ or O^+ are not distinguished and depend on the details of the ion chemistry near the critical level. We introduce a factor f that is the total local ion production ($P \approx I_O n_n$) going into O^+ after chemistry is taken into account. The rest of the ion production, with the fraction $(1 - f)$, is assumed to become O_2^+. Recall that the O_2^+ comes from the chemical reaction (equation (4)) of O^+ with CO_2.

We can now, with some degree of inconsistency, combine equation (20) with the critical neutral densities for O_2^+ and O^+, found earlier, to obtain global loss rates for these species. The factors f and $(1 - f)$ for O^+ and O_2^+, respectively, were thrown in so that the ion production rate was not double counted. Admittedly, this is bit ad hoc. The overall dayside ion loss rate (to the night or lost from Mars) from ionization is then very roughly

$$\begin{aligned} Q_{O2+} &\approx 3 \times 10^{24} s^{-1}(1-f)(I/I_{Ox0})^{1/2}(p_{sw}/p_{sw0})^{1/2} \\ Q_{O+} &\approx 4 \times 10^{24} s^{-1} f (I/I_{Ox0})^{6/7}(p_{sw}/p_{sw0})^{2/7} \end{aligned} \tag{32}$$

Note that the ionization frequency ratio, I/I_{Ox0}, is roughly $F_{10.7}/200$. The total O atom transport loss from Mars due to ion loss is $Q_{ion} = 2Q_{O2+} + Q_{O+}$.

The fraction f depends on altitude (or neutral density) via the critical neutral densities defined above, but we make the additional approximation of evaluating f at just the O^+ neutral critical density from equation (29). The O_2^+ and O^+ critical neutral densities are very similar so this assumption makes little difference. Taking the fraction f as $f = n_{O+}/(n_{O+} + n_{O2+})$ and using photochemical expressions for the ion densities derived earlier gives

$$f = 1/\left\{1 + (k_4 k_c/2\alpha)\, n_n^{3/2}\right\} \approx 0.5 \tag{33}$$

Note that $f \approx 0.5$ for the MAVEN epoch. The Q_{ion} expression can now be evaluated. At the reference values of solar wind pressure and solar EUV irradiance we find that $Q_{ion} \approx (0.4 \times 3 + 0.8 \times 4) \times 10^{24}$ s^{-1} $\approx 4 \times 10^{24}$ s^{-1}. However, it would probably be reasonable to just use equation (20) and a compromise O^+/O_2^+ critical neutral density, which also gives an overall ion loss rate of $\approx 4 \times 10^{24}$ s^{-1} for the current epoch.

Q_{ion} is about 5–10% of the total O loss from photochemistry (cf. Lillis et al., 2017; Cravens et al., 2017, and references therein). Of more interest is the variation with solar EUV irradiance and with upstream solar wind pressure (i.e., variation goes as the square root). For comparison, the photochemical loss rate varies linearly with the solar EUV irradiance according to Cravens et al. (2017). The equation (32) values of the global escape rates are roughly consistent with results from global simulations and from data analysis (cf. Brain et al., 2015). Lundin et al. (2013) found using MGS data that the heavy ion (O^+ and O_2^+) escape rate varied approximately linearly with $F_{10.7}$.

Note that all the above analysis applies to draped magnetic field regions and not to the crustal magnetic field regions. Regions of the ionosphere containing strong crustal magnetic fields are shielded to a large extent from solar wind effects, and ion transport should be largely parallel to the magnetic field. All such ions should sooner or later be photochemically processed, even those ions created at high altitudes, and thus eventually contribute to the photochemical neutral O loss in crustal field regions (see Cravens et al., 2017). Another limitation of our results is that in order to derive the plasma flow speeds needed to find the transport time constants and critical neutral densities flow parallel to the magnetic field purely due to the thermal pressure gradient was not taken into account. One effect of this is that the plasma flow from day to night is not azimuthally symmetric but depends on the orientation of the draped magnetic field. This might reduce the net ion loss from the dayside by as much as a factor of 2 due to the lower flow speeds parallel to the field.

6. Conclusions

Simple analytical and semiempirical expressions for ion flow speeds and ion loss were derived. MAVEN data were used as input for the estimates. Typical ion flow speeds are found to be about 1 km/s in the dayside topside ionosphere near an altitude of 300–400 km, and, not surprisingly, the flow speed increases with altitude. In agreement with more sophisticated models and with purely empirical studies, we found that the oxygen loss rate due to ion transport is about 5% (i.e., a global O ion loss rate of $Q_{ion} \approx 4 \times 10^{24}$ s^{-1}) of the total oxygen loss rate. The global ion loss rate is found to vary linearly with the solar EUV irradiance and as the square root of the solar wind dynamic pressure. The estimates and simple MHD arguments that were made in this paper are not meant to be quantitatively accurate or to replace more sophisticated numerical models, but they should be able to help interpret these models as well as help to interpret MAVEN data.

Acknowledgments
MAVEN data are available in the Planetary Data System. All data shown in the figures can be obtained from the corresponding author. This work was supported at the University of Kansas by NASA grant NNH10CC04C to the University of Colorado and by subcontract to the University of Kansas. The MAVEN project is supported by NASA through the Mars Exploration Program.

References

Akalin, F., Morgan, D. D., Gurnett, D. A., Kirchner, D. L., Brain, D. A., Modolo, R., … Espley, J. R. (2010). Dayside induced magnetic field in the ionosphere of Mars. *Icarus*, *206*, 104–111. https://doi.org/10.1016/j.icarus.2009.03.021

Benna, M., Mahaffy, P. R., Grebowsky, J. M., Fox, J. L., Yelle, R. V., & Jakosky, B. M. (2015). First measurements of composition and dynamics of the Martian ionosphere by MAVEN's Neutral Gas and Ion Mass Spectrometer. *Geophysical Research Letters*, *42*, 8958–8965. https://doi.org/10.1002/2015GL065146

Bougher, S. W., Cravens, T. E., Grebowsky, J., & Luhmann, J. (2015). The aeronomy of Mars: Characterization by MAVEN of the upper atmosphere reservoir that regulates volatile escape. *Space Science Reviews*, *195*, 423. https://doi.org/1007/s11214-014-0053-7

Bougher, S. W., Pawlowski, D., Bell, J., Nelli, S., McDunn, T., Murphy, J., … Ridley, A. (2015). Mars Global Ionosphere Thermosphere Model (M-GITM): I. Solar cycle, seasonal, and diurnal variations of the upper atmosphere. *Journal of Geophysical Research Planets*, *120*, 311–342. https://doi.org/10.1002/2014JE004715

Brain, D. A., McFadden, J. P., Halekas, J. S., Connerney, J. E. P., Bougher, S. W., Curry, S., … Seki, K. (2015). The spatial distribution of planetary ion fluxes near Mars observed by MAVEN. *Geophysical Research Letters*, *42*, 9142–9148. https://doi.org/10.1002/2015GL065293

Brecht, S. H., & Ledvina, S. A. (2014). The role of the Martian crustal magnetic fields in controlling ionospheric loss. *Geophysical Research Letters*, *41*, 5340–5346. https://doi.org/10.1002/2014GL060841

Connerney, J. E. P., Espley, J. R., Bracio, G. A. D., Gruesbeck, J. R., Oliverson, R. J., Mitchell, D. L., … Jakosky, B. M. (2015). First results of the MAVEN magnetic field investigation. *Geophysical Research Letters*, *42*, 8828–8827. https://doi.org/10.1002/2015GL065248

Cravens, T. E. (1997). *Physics of Solar System Plasmas*. UK: Cambridge University Press.

Cravens, T. E., Rahmati, A., Fox, J. L., Lillis, R., Bougher, S., Luhmann, J., … Jakosky, B. (2017). Hot oxygen escape from Mars: Simple scaling with solar EUV irradiance. *Journal of Geophysical Research: Space Physics*, *122*, 1102–1116. https://doi.org/10.1002/2016JA023461

Cravens, T. E., Richard, M., Ma, Y.-J., Bertucci, C., Luhmann, J., Ledvina, S., … Ulusen, D. (2010). Dynamical and magnetic field time constants for Titan's ionosphere—Empirical estimates and comparisons with Venus. *Journal of Geophysical Research*, *115*, A08319. https://doi.org/10.1029/2009JA015050

Crider, D. H., Acuna, M. H., Connerney, J. E. P., Vignes, D., Ness, N. F., Krymskii, A. M., … Winterhalter, D. (2002). Observations of the latitude dependence of the location of the Martian magnetic pileup boundary. *Geophysical Research Letters*, *29*(8), 1170. https://doi.org/10.1029/2001GL013860.

Crider, D. H, Vignes, D., Krymskii, A. M., Breus, T. K., Ness, N. F., Mitchell, D. L., Slavin, J. A., & Acuna, M. (2003). A proxy for determining solar wind pressure at Mars using Mars Global Surveyor data. *Journal of Geophysical Research*, *108*(A12), 1461. https://doi.org/10.1029/2003JA009875.

Dong, C., Bougher, S. W., Ma, Y., Toth, G., Nagy, A. F., & Najib, D. (2014). Solar wind interaction with Mars upper atmosphere: Results from the one-way coupling between the multi-fluid MHD model and the MTGCM model. *Geophysical Research Letters*, *41*, 2708–2715. https://doi.org/10.1002/2014GL059515

Edberg, N. J. T., Brain, D. A., Lester, M., Cowley, S. W. H., Modolo, R., Fränz, M., & Barabash, S. (2009). Plasma boundary variability at Mars as observed by Mars Global Surveyor and Mars Express. *Annales de Geophysique*, *27*, 3537. https://doi.org/10.5194/angeo-27-3537-2009

Ergun, R. E., Andersson, L., Fowler, C. M., Woodson, A. K., Weber, T. D., Delory, G. T., … Jakosky, B. M. (2016). Enhanced O_2^+ loss at Mars due to an ambipolar electric field from electron heating. *Journal of Geophysical Research: Space Physics*, *121*, 4668–4678. https://doi.org/10.1002/2016JA022349

Ergun, R. E., Morooka, M. W., Andersson, L. A., Fowler, C. M., Delory, G. T., Andrews, D. J., … Jakosky, B. M. (2015). Dayside electron temperature and density profiles at Mars: First results from the MAVEN Langmuir probe and waves instrument. *Geophysical Research Letters*, *42*, 8846–8853. https://doi.org/10.1002/2015GL065280

Fox, J. L. (1997). Upper limits to the outflow of ions at Mars: Implications for atmospheric evolution. *Geophysical Research Letters*, *24*, 2901–2904. https://doi.org/10.1029/97GL52842

Fox, J. L. (2009). Morphology of the dayside ionosphere of Mars: Implication for ion outflows. *Journal of Geophysical Research*, *114*, E12005. https://doi.org/10.1029/2009JE003432

Fox, J. L., & Hać, A. B. (2014). The escape of O from Mars: Sensitivity to the elastic cross sections. *Icarus*, *228*, 375. https://doi.org/10.1016/j.icarus.2013.10.014

Fox, J. L., Benna, M., Mahaffy, P. R., & Jakosky, B. M. (2015). Water and water ions in the Martian thermosphere/ionosphere. *Geophysical Research Letters*, *42*, 8977–8985. https://doi.org/10.1002/2015GL065465

Fränz, M., Dubinin, E., Nielsen, E., Woch, J., Barabash, S., Lundin, R., & Fedorov, A. (2010). Transterminator ion flow in the Martian ionosphere. *Planetary and Space Science*, *58*, 1442.

Jakosky, B. M., Grebowsky, J. M., Luhmann, J. G., & Brain, D. A. (2015). Initial results from the MAVEN mission to Mars. *Geophysical Research Letters*, *42*, 8791–8802. https://doi.org/10.1002/2015GL065271

Lillis, R. J., Brain, D. A., Bougher, S. W., Leblanc, F., Luhmann, J. G., Jakosky, B. M., … Lin, R. P. (2015). Characterizing atmospheric escape from Mars today and through time, with MAVEN. *Space Science Reviews*, *195*, 357. https://doi.org/10.1007/s11214-015-0165-8

Lillis, R. J., Deighan, J., Fox, J., Bougher, S., Lee, Y., Combi, M., … Chaufray, J.-Y. (2017). Photochemical escape of oxygen from Mars: First results from MAVEN in situ data. *Journal of Geophysical Research: Space Physics*, *122*, 3815–3836. https://doi.org/10.1002/2016JA023525

Lundin, R., Barabash, S., Holmstrom, M., Nilsson, H., Futaana, Y., Ramstad, R., … Fraenz, M. (2013). Solar cycle effects on the ion escape from Mars. *Geophysical Research Letters*, *40*, 6028–6032. https://doi.org/10.1002/2013GL058154

Ma, Y., Nagy, A. F., Sokolov, I. V., & Hansen, K. C. (2004). Three-dimensional, multispecies, high spatial resolution MHD studies of the solar wind interaction with Mars. *Journal of Geophysical Research*, *109*, A07211. https://doi.org/10.1029/2003JA010367

Ma, Y. J., Russell, C. T., Fang, X., Dong, Y., Nagy, A. F., Toth, G., … Jakosky, B. M. (2015). MHD model results of solar wind interaction with Mars and comparison with MAVEN plasma observations. *Geophysical Research Letters*, *42*, 9113–9120. https://doi.org/10.1002/2015GL065218

Mahaffy, P. R., Benna, M., King, T., Harpold, D. N., Arvey, R., Barciniak, M., … Nolan, J. T. (2015). The neutral gas and ion mass spectrometer on the Mars atmosphere and volatile evolution mission. *Space Science Reviews*, *195*, 49. https://doi.org/10.1007/s11214-014-0091-1

Matta, M., Withers, P., & Mendillo, M. (2013). The composition of Mars' topside ionosphere: Effects of hydrogen. *Journal of Geophysical Research*, *118*, 2681–2693. https://doi.org/10.1002/jgra.50104

McFadden, J. P., Livi, R., Luhmann, J., Connerney, J., Mitchell, D., Mazelle, C., … Jakosky, B. (2015). Structure of the Martian ionosphere and atmospheric loss: MAVEN STATIC first results. Lunar Planet. Sci. Conf. Abstract 2899.

Modolo, R., Hess, S., Mancini, M., Leblanc, F., Chaufray, J.-Y., Brain, D., … Mazelle, C. (2016). Mars-solar wind interaction: LatHyS, an improved parallel 3-D multispecies hybrid model. *Journal of Geophysical Research*, *121*(7), 6378–6399. https://doi.org/10.1002/2015JA022324

Peverall, R., Rosén, S., Peterson, J. R., Larsson, M., Al-Khalili, A., Vikor, L., … van der Zande, W. J. (2001). Dissociative recombination and excitation of O_2^+: Cross sections, product yields and implications for studies of ionospheric airglows. *The Journal of Chemical Physics*, *114*, 6679. https://doi.org/10.1063/1.1349079

Rahmati, A., Larson, D. E., Cravens, T. E., Lillis, R. J., Dunn, P. A., Halekas, J. S., … Jakosky, B. M. (2015). MAVEN insights into oxygen pickup ions at Mars. *Geophysical Research Letters*, *42*, 8870. https://doi.org/10.1002/2015GL065262

Sakai, S., Andersson, L., Cravens, T. E., Mitchell, D. L., Mazelle, C., Rahmati, A., … Jakosky, B. M. (2016). Electron energetics in the Martian dayside ionosphere: Model comparisons with MAVEN data. *Journal of Geophysical Research: Space Physics*, *121*, 7049–7066. https://doi.org/10.1002/2016JA022782

Sakai, S., Rahmati, A., Mitchell, D. L., Cravens, T. E., Bougher, S. W., Mazelle, C., … Jakosky, B. M. (2015). Model insights into energetic photoelectrons measured at Mars by MAVEN. *Geophysical Research Letters*, *42*, 8894. https://doi.org/10.1002/2015GL065169

Schunk, R. W., & Nagy, A. F. (2009). *Ionospheres: Physics, Plasma Physics, and Chemistry* (2nd Ed.). UK: Cambridge University Press.

Shinagawa, H., & Cravens, T. E. (1989). A one-dimensional multispecies MHD model of the dayside ionosphere of Mars. *Journal of Geophysical Research*, *94*, 6506.

Withers, P., Vogt, M., Mayyasi, M., Mahaffy, P., Benna, M., Elrod, M., … Jakosky, B. (2015). Comparison of model predictions for the composition of the ionosphere of Mars to MAVEN NGIMS data. *Geophysical Research Letters*, *42*, 8966. https://doi.org/10.1002/2015GL065205